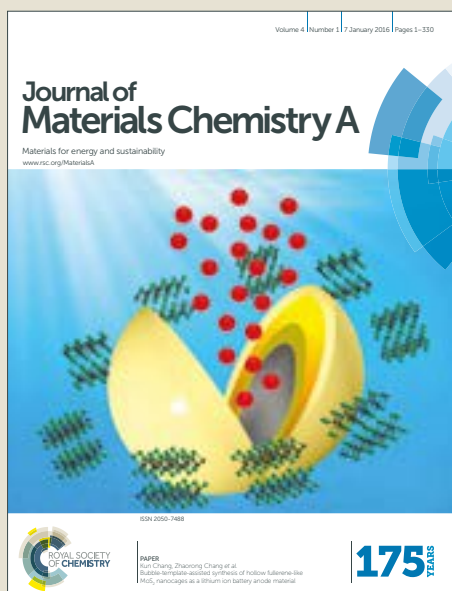


Journal of Materials Chemistry A

Accepted Manuscript



This article can be cited before page numbers have been issued, to do this please use: G. Chen, L. Zhang, Y. Zhang, K. Liu, Z. Long and Y. Wang, *J. Mater. Chem. A*, 2019, DOI: 10.1039/C8TA12562G.



This is an Accepted Manuscript, which has been through the Royal Society of Chemistry peer review process and has been accepted for publication.

Accepted Manuscripts are published online shortly after acceptance, before technical editing, formatting and proof reading. Using this free service, authors can make their results available to the community, in citable form, before we publish the edited article. We will replace this Accepted Manuscript with the edited and formatted Advance Article as soon as it is available.

You can find more information about Accepted Manuscripts in the [author guidelines](#).

Please note that technical editing may introduce minor changes to the text and/or graphics, which may alter content. The journal's standard [Terms & Conditions](#) and the ethical guidelines, outlined in our [author and reviewer resource centre](#), still apply. In no event shall the Royal Society of Chemistry be held responsible for any errors or omissions in this Accepted Manuscript or any consequences arising from the use of any information it contains.

Targeted synthesis of ionic liquid-polyoxometalates derived Mo-based electrodes for advanced electrochemical performance

Guojian Chen,^{*a} Lei Zhang,^b Yadong Zhang,^a Ke Liu,^a Zhouyang Long^a and Ying Wang^{*a}

Received 00th January 20xx,
Accepted 00th January 20xx

DOI: 10.1039/x0xx00000x

www.rsc.org/

Rational design of advanced electrode materials with high capacity and long cycle stability is a great challenge for both lithium and sodium storage. In this work, we report a versatile strategy for the synthesis of N/P-codoped MoO₂@carbon (N/P-MoO₂@C) electrodes via a simple pyrolysis of ionic liquid-based polyoxometalate (IL-POM) molecular precursors. The contents of C, N, and P, and the pore geometry of N/P-MoO₂@C networks can be easily tailored by adjusting the position of cyano groups in the IL-POMs precursor. Benefiting from this novel design, the optimized N/P-MoO₂@C4 electrode with cross-linked porous tunnels and abundant defects exhibits excellent lithium storage performance, with a high reversible capacity of 1381 mAh g⁻¹ after 100 cycles at 0.5 A⁻¹, and 346 mAh g⁻¹ after 5000 cycles at 20 A g⁻¹. The Li⁺ storage performance of this N/P-MoO₂@C4 is dominated by pseudocapacitance behavior, which attributed to the high reversible capacity and long cycle stability. Exceptional sodium storage performance is also observed in the N/P-MoO₂@C4 electrode with 0.02% capacity decay per cycle over 1100 cycles at 1.0 A g⁻¹. The present approach provides some insight into design and synthesis of task-specific Mo-based materials towards the applications in energy storage and conversion.

Introduction

Lithium ion batteries (LIBs) have been widely used in various portable devices and smart grids, owing to their high energy density and environmentally friendly behavior.¹ The constantly growing requirements arising from high-performance electronic devices are dependent on the further innovations on LIBs in terms of higher energy/power density, longer cycling performance, and lower cost.^{2,3} Traditional anode material of graphite, however, fails to fulfill all these requirements due to its low theoretical capacity (372 mAh g⁻¹). Recently, sodium ion batteries (SIBs) have also received ever-increasing attention as alternatives to LIBs due to their similar chemical mechanism and the Earth's abundant resources of sodium.⁴ Compared to LIBs, the larger and heavier Na⁺ generally results a more sluggish kinetics in SIBs, which results in poor rate performance and low utilization of active materials. In both cases, rational design of electrode materials with high reversible capacity and long cycle-life is highly urgent.

As a typical conversion-type material, MoO₂ demonstrates huge potential for both LIBs and SIBs due to its high theoretical capacity and good conductivity (8.8 × 10⁻⁵ Ω cm).⁵ Unfortunately, the strong Mo-O bond and slow electron transport kinetics of bulk MoO₂ generally lead to low specific capacity (210 mAh g⁻¹ in LIBs) and poor rate capability.⁵ Moreover, the large volume expansion/shrinkage of

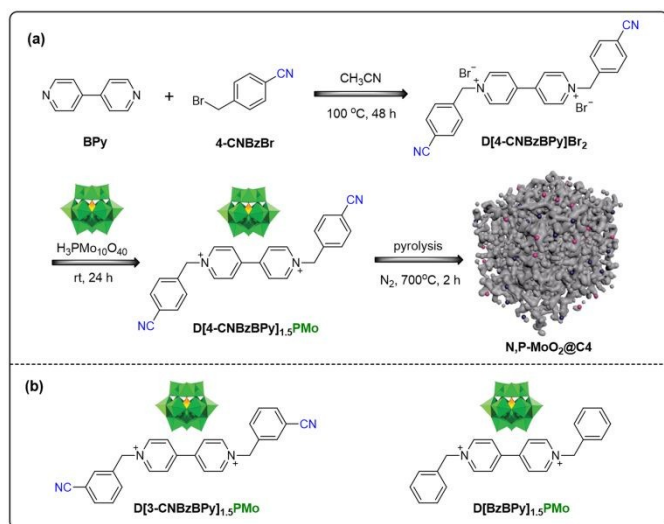
MoO₂ during electrochemical cycling result in large irreversible capacity decay. To date, many efforts have been made to address the above issues (*i.e.* fabricating nanostructured MoO₂ and hybridizing MoO₂ with carbon).⁵⁻⁸ Especially, MoO₂/carbon hybrids have demonstrated an improved Li-insertion kinetics and a well cycle stability.⁹⁻¹⁴ It is still a huge challenge, however, to achieve attractive high capacity and long-term cycle stability at high current densities.

Herein, a novel strategy to dramatically improve the electrochemical performance of MoO₂ is proposed, based on constructing ionic liquid-polyoxometalate derived N/P-codoped MoO₂@carbon mesoporous networks (denoted as N/P-MoO₂@C), as demonstrated in Scheme 1. To the best of our knowledge, the present N/P-MoO₂@C hybrids have never been reported for lithium or/and sodium storage. Fortunately, recent reports have revealed some scientific clues that make this electrode attractive: (1) The cross-linked conductive networks that formed by MoO₂ skeleton and carbon layers can provide multidimensional channels for efficient electron/ion transport, thus promoting the electrochemical kinetics.¹¹⁻¹⁴ (2) Synergetic effects between N and P codoping within MoO₂ and the carbon can generate more defects, vacancies, and bifunctional active sites to facilitate better electrochemical performance, as has been revealed in other electronic devices.¹⁵⁻¹⁸ (3) The porous geometry of the designed networks can not only tolerate the volume changes of MoO₂, but also provide better contact between the electrolyte and electrode, thus enhancing the structural stability and shortening ion diffusion pathways.^{5,11,13,14} Therefore, seeking a suitable method to synthesize N/P-MoO₂@C networks is of great scientific and practical importance.

^a School of Chemistry and Materials Science, Jiangsu Key Laboratory of Green Synthetic Chemistry for Functional Materials, Jiangsu Normal University, Xuzhou 221116, China. E-mail: gjchen@jsnu.edu.cn; yingwang@jsnu.edu.cn

^b Centre for Clean Environment and Energy, Griffith University, Queensland 4222, Australia

Electronic Supplementary Information (ESI) available: [details of any supplementary information available should be included here]. See DOI: 10.1039/x0xx00000x



Scheme 1 (a) Schematic illustration of the bottom-up preparation of the N/P-MoO₂@C4 network by direct pyrolysis of the IL-POM precursor, D[4-CNzBPY]_{1.5}PMo, that is self-assembled from 4-cyano-tethered viologen IL precursor designed on the molecular scale with H₃PMo₁₂O₄₀. (b) Other control IL-POM precursors with the adjustable 3-cyano-groups or cyano-free IL cations.

Ionic liquid-based polyoxometalates (IL-POMs) are organic-inorganic hybrid materials that combine diverse IL cations with POM anions,^{19–21} which have been used as heterogeneous catalysts.²² IL-POM-derived Mo-based electrode materials have never been reported, however. In this work, for the first time, well-designed IL-POMs are used as molecular precursors to synthesize N/P-MoO₂@C electrodes. Novel mesoporous IL-POM ionic hybrids were self-assembled between newly-designed cyano-tethered viologen IL cations and commercial H₃PMo₁₂O₄₀ (Scheme 1). After the pyrolysis, a MoO₂ skeleton derived from PMo₁₂O₄₀³⁻ anions is generated. In addition, the introduced N/P heteroatoms and carbon layers originated from the cyano-tethered viologen IL cations and the P-centered POM anions. By simply adjusting the positions of cyano groups in the IL-POMs, we constructed a series of N/P-MoO₂@C samples with controllable contents of C, N, and P, and controllable pore geometry. The optimized sample N/P-MoO₂@C4 exhibited outstanding electrochemical performance for both LIBs and SIBs, with long-life cycling stability, high rate capability, and high reversible capacity.

Results and discussion

Scheme 1a depicts the synthetic procedure of the typical N/P-MoO₂@C4 network. First, cyano-tethered viologen IL (D[4-CNzBPY]Br₂) is prepared by quaternization reaction between 4,4'-bipyridine and 4-cyanobenzyl bromide, and then D[4-CNzBPY]_{1.5}PMo is synthesized by the ionic self-assembly of D[4-CNzBPY]Br₂ with equivalent H₃PMo₁₂O₄₀ in aqueous solution. The targeted N/P-MoO₂@C4 network is fabricated by direct pyrolysis of D[4-CNzBPY]_{1.5}PMo at 700 °C for 2 h under a N₂ atmosphere. By varying the IL-POM molecular precursors D[3-CNzBPY]_{1.5}PMo and D[BzBPY]_{1.5}PMo (Scheme 1b), distinct N/P-MoO₂@C3 and N/P-MoO₂@C0 networks were prepared. The chemical structures and compositions of the above ILs and IL-POMs were confirmed by ¹H

nuclear magnetic resonance (NMR), ¹³C NMR, elemental analysis, and Fourier transform infrared (FTIR) spectroscopy (see Fig. S1–S4, ESI). The most obvious distinction between these IL-POMs depends on the different molecular structures related to the positions (3 or 4) of cyano-groups in the IL cations or whether the material is cyano-free (denoted by 0), which leads to the differences in pore geometry and thermal stability between the IL-POMs presented later.

The scanning electron microscopy (SEM) image (Fig. 1a) reveals that D[4-CNzBPY]_{1.5}PMo consists of fluffy sponge-like three-dimensional (3D) mesoporous networks. Similar morphologies are also observed in the D[3-CNzBPY]_{1.5}PMo and D[BzBPY]_{1.5}PMo (Fig. S5, ESI). The uniformly distributed cyano-tethered viologen organic cations and PMo nanoclusters in IL-POM hybrids allow *in-situ* generation of N/P-MoO₂@C networks. After the annealing process, the sponge-like 3D mesoporous morphology is well preserved in the resulting N/P-MoO₂@C4 network. Meanwhile, the decomposition and release of IL cations leads to the formation of an intercross-linked structure that is composed of some tightly packed nanorods (Fig. 1b). The cross-linked structure of N/P-MoO₂@C4 networks is confirmed by transmission electron microscopy (TEM) image in Fig. 1c, which shows abundant mesopores originated from nanovoids between interconnected nanoparticles, in accordance with the SEM image. Typical lattice fringes with spacing of 0.34 nm for the (-111) plane of MoO₂ and some amorphous carbons are observed in the high-resolution TEM (HR-TEM) image (Fig. 1d). Compared to N/P-MoO₂@C4, the network structure of N/P-MoO₂@C0 is relatively loose (see SEM image in Fig. S5 and TEM image in Fig. S6).

A comprehensive analysis of the pore structures of D[4-CNzBPY]_{1.5}PMo and N/P-MoO₂@C4 was carried out by N₂ sorption experiments. Fig. 1f and Fig. S7 show that the adsorption isotherms are all type IV with H1-type hysteresis loops in the high relative pressure (*P/P*₀) range from 0.5 to 0.9, indicative of typical mesoporous materials.^{20,21} All the textural properties of IL-POMs and their derived networks are listed in Table S1. The typical D[4-CNzBPY]_{1.5}PMo has a desirable Brunauer-Emmett-Teller (BET) surface areas of 63 m² g⁻¹ with a large pore volume of 0.37 cm³ g⁻¹. After the pyrolysis, N/P-MoO₂@C4 shows a higher BET surface area of 89 m² g⁻¹ with a declining pore volume of 0.16 cm³ g⁻¹ that is due to its compact cross-linked network. Besides, both D[4-CNzBPY]_{1.5}PMo and N/P-MoO₂@C4 have some micropore surface areas (Table S1, ESI), indicating the existence of a small amount of micropores. The Barrett-Joyner-Halenda (BJH) pore size distribution curves (Fig. 1g) also show that the most probable pore diameters have changed from 19.0 nm for D[4-CNzBPY]_{1.5}PMo to smaller mesopores centered at 3.5 nm for N/P-MoO₂@C4, demonstrating its small-size mesoporous structure. As shown in Fig. S8, the NLDFT pore size distribution further confirms that a small amount of micropores appear at 1.4 nm and enriched small mesopores appear at 4.3 nm, which is consistent with the results in Table S1 and Fig. 1g. The control samples D[3-CNzBPY]_{1.5}PMo and D[BzBPY]_{1.5}PMo possess similar surface areas and pore volumes with D[4-CNzBPY]_{1.5}PMo, but their pyrolyzed products N/P-MoO₂@C3 and N/P-MoO₂@C0 have obviously different surface area of 28 and 51 m² g⁻¹, respectively, with low pore volumes and larger mesopore sizes (Table S1). The above difference is attributed to the tailored molecular structures of the IL cations, which were achieved by

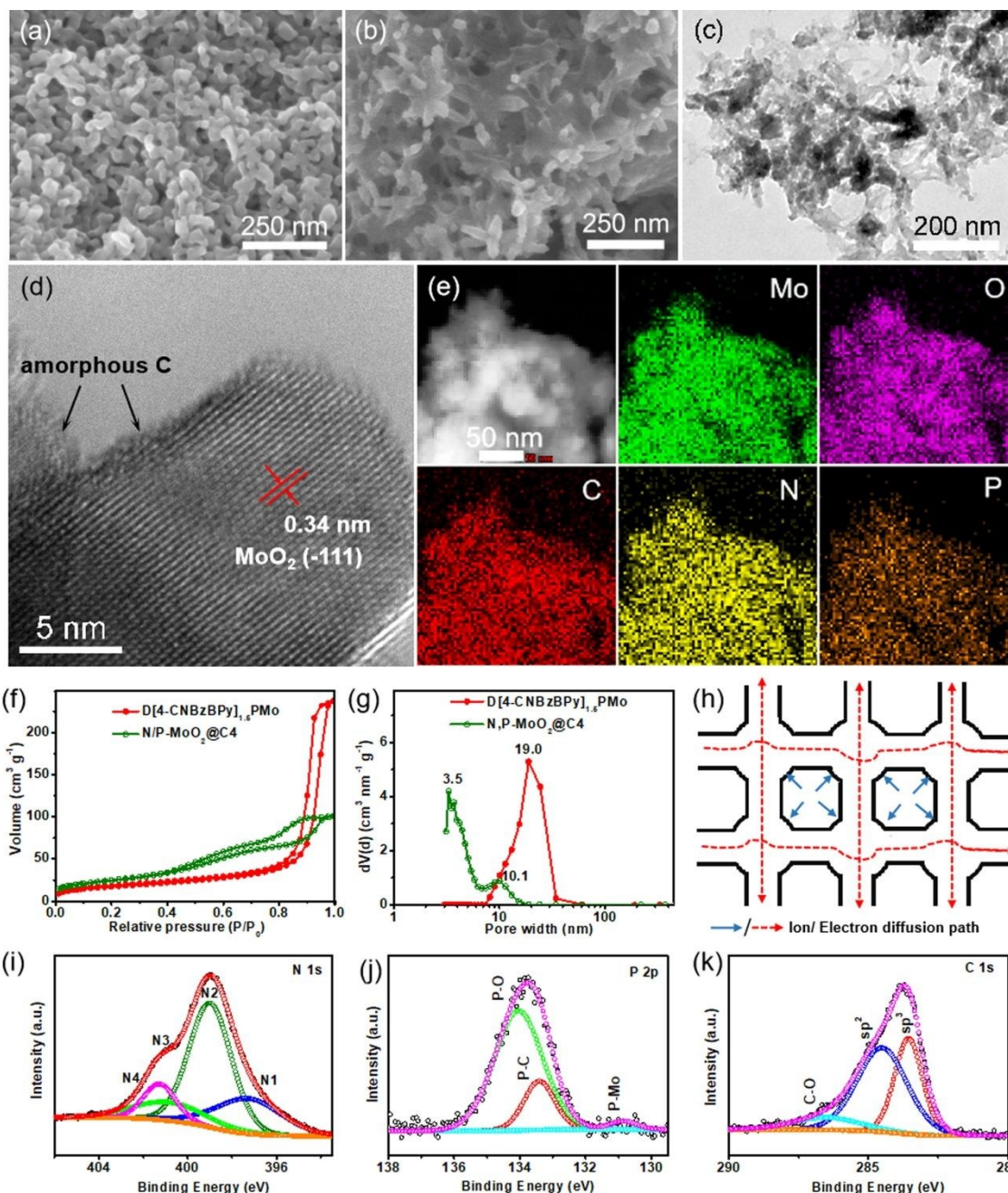


Fig. 1 SEM images of (a) D[4-CNzBzBPyl]₅PMo and (b) N/P-MoO₂@C₄. (c) TEM and (d) HR-TEM images of N/P-MoO₂@C₄. (e) STEM EDS elemental mapping of Mo, O, C, N and P in the N/P-MoO₂@C₄ at the nanoscale (50 nm). (f) N₂ sorption isotherms and (g) BJH pore size distributions of D[4-CNzBzBPyl]₅PMo and N/P-MoO₂@C₄. (h) Illustration of ion/electron diffusion paths of the N/P-MoO₂@C₄. (i) N 1s, (j) C 1s, and (k) P 2p XPS spectra of N/P-MoO₂@C₄.

varying the positions of cyano groups. The structural advantage of this cross-linked N/P-MoO₂@C₄ network is illustrated in Fig. 1h. The tightly-packed cross-linked porous structure not only enables shorter ion diffusion pathways, but also makes the electron diffusion happen

in multiple directions, which allows more electrons to pass in a given time. Compared to N/P-MoO₂@C₄, N/P-MoO₂@C₀ has a relatively loose network, which indicates longer ion diffusion pathways and less directions for electron diffusion. Therefore, N/P-MoO₂@C₄

provides multiple channels for faster electron/ion transport, as confirmed by a lower charge transfer resistance in Fig. S9.

XRD patterns of the IL-POM precursors and their derivatives are shown in Fig. S10. The D[4-CNzBPY]_{1.5}PMo shows a broad Bragg peak that appears at 8.30° with a *d*-spacing of 1.06 nm, indicating that PMo clusters (~1.0 nm) are uniformly dispersed in the IL-POM networks in a certain regular ion-pair array.^{20,21} XRD pattern (Fig. S10b, ESI) of the as-synthesized N/P-MoO₂@C4 matches well with standard monoclinic MoO₂ peaks (JCPDS No. 32-671), demonstrating the formation of high purity MoO₂ only with small amount of amorphous carbons by the degradation of IL-POMs. As for the control samples, D[BzBPY]_{1.5}PMo gives a similar N/P-MoO₂@C0 network, but D[3-CNzBPY]_{1.5}PMo changes to a N/P-MoO₂C@C3 network (Fig. S10c), which caused by their distinct thermal stabilities (Fig. S11, ESI). The above results imply that IL-POM derived materials can be easily tailored on molecular-scale by simply varying the positions of cyano groups in the IL cations. Raman spectroscopy (Fig. S12, ESI) was further employed to clarify the chemical components of the N/P-MoO₂@C4 and N/P-MoO₂@C0 networks. The characteristic peaks for monoclinic MoO₂ are observed at 282, 337, 662, 819, and 992 cm⁻¹.^{1,7,13} The broad band at 1348 cm⁻¹ is the D band that associates with *sp*³-type disordered carbon, and the band at 1606 cm⁻¹ is assigned to the G band derived from *sp*²-type graphitic carbon.^{7,13} The intensity ratios of the D to the G band (*I*_D/*I*_G) are 1.07 and 1.05 for N/P-MoO₂@C4 and N/P-MoO₂@C0, respectively, which are higher than other reported carbon materials.^{13,23-25} The higher *I*_D/*I*_G values in these N/P-MoO₂@C networks not only confirm the existence of amorphous carbons in both samples, but also indicate more defects and disorders, which is favorable for enhancing the electrical and ionic transport of the electrode.⁵ The *I*_D/*I*_G value of N/P-MoO₂@C4 is higher than that of N/P-MoO₂@C0, demonstrating more structural defects (e.g. voids and holes) and disorders in the carbon layers.

Further investigation about the electronic states of N/P-MoO₂@C4 was performed by X-ray photoelectron spectroscopy (XPS, Fig. 1i-1k). Besides the Mo, O, and C, the XPS survey (Fig. S13, ESI) shows obvious signals for N and P, indicating that N and P were successfully introduced into the networks. The N 1s plot shows four typical peaks for the N-Mo bonds (N1 at 397.4 eV),²⁶ pyridinic N (N2 at 399.0 eV), pyrrolic N (N3 at 400.7 eV), and graphitic N (N4 at 401.3 eV), respectively.^{17,27} The P 2p plot shows two dominant peaks at 133.4 and 134.1 eV, corresponding to the P-O and P-C bonds.¹⁶⁻¹⁸ Since the P-C bond (1.77 Å) is much larger than the C-C *sp*² bond (1.42 Å), the doped-P can induce structural distortion and introduce more defects into the carbon matrix,^{17,18} in accordance with the Raman results. The P-Mo bond is observed at 130.8 eV, confirming partial P doping within the MoO₂ structure.^{17,18} The C 1s spectrum contains three peaks at 283.5, 284.7, and 286.9 eV, corresponding to *sp*³-C, *sp*²-C, and C-O bond, respectively.^{18,27} The XPS results confirm that N and P are codoped into both MoO₂ and carbon. A similar chemical state is also observed in the N/P-MoO₂@C0 sample (Fig. S14, ESI).

The energy dispersive spectroscopy (EDS) elemental mapping images performed both in the SEM mode (Fig. S15 and S16, ESI) and the scanning TEM (STEM) mode (Fig. 1e and Fig. S6c) display uniform distributions of Mo, O, C, N, and P elements for the N/P-MoO₂@C4 and N/P-MoO₂@C0, from the micrometer scale to nanoscale. The contents of MoO₂ in N/P-MoO₂@C4 and N/P-MoO₂@C0 are determined to be 86.1 and 88.2 wt%, calculated based on the TGA

results collected in air (Fig. S17, ESI). The C and N content in each sample is obtained based on elemental analysis, and P content is calculated based on (100-wt_{MoO₂}-wt_C-wt_N)%. Detailed elemental compositions of N/P-MoO₂@C4 and N/P-MoO₂@C0 are shown in Table S2. Apparently, the N/P-MoO₂@C4 shows a higher content of C (5.2 wt%), N (1.8 wt%), and P (6.9 wt%), compared with that of N/P-MoO₂@C0. The above results suggest that the N, P and C doping levels in the resultant samples can be elaborately tailored by adjusting the molecular structures of IL cations.

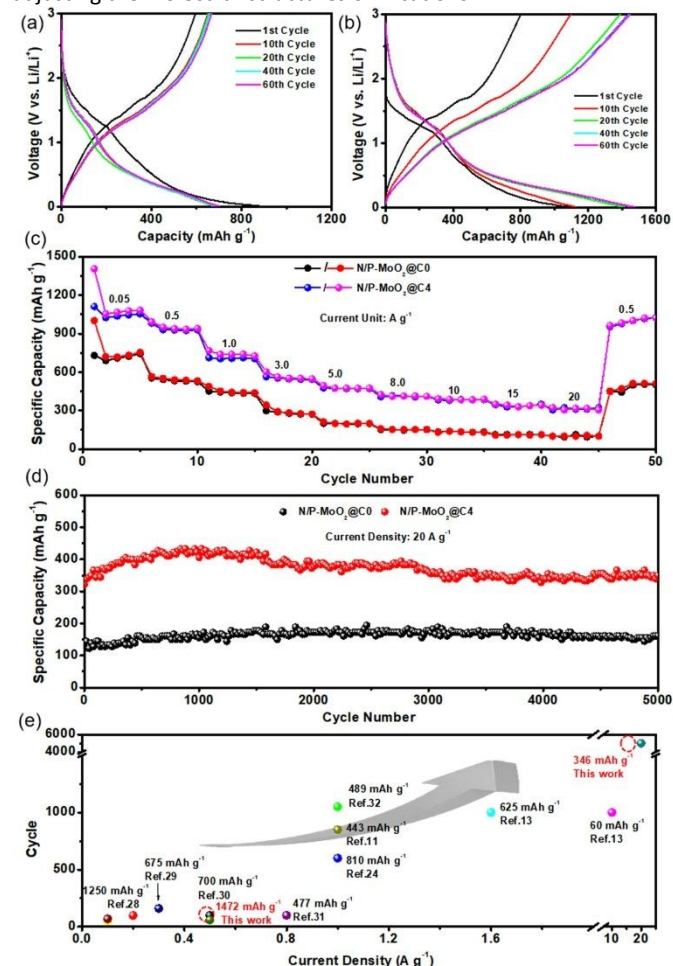


Fig. 2 Lithium storage performances of the synthesized N/P-MoO₂@C networks. (a, b) Charge-discharge profiles of N/P-MoO₂@C0 and N/P-MoO₂@C4 at 0.5 A g⁻¹, respectively. (c) Rate performance at various current densities, from 0.05 to 20 A g⁻¹ and then back to 0.5 A g⁻¹, and (d) long-life cycling performance at 20 A g⁻¹. (e) Electrochemical performance comparison of N/P-MoO₂@C4 with other high quality MoO₂-based electrode.

Lithium storage performance of the N/P-MoO₂@C networks is determined by assembling 2032 half-cells. Fig. 2a and 2b compares the discharge/charge profiles of N/P-MoO₂@C4 and N/P-MoO₂@C0 at 0.5 A g⁻¹. Clearly, the electrode N/P-MoO₂@C4 delivers a higher initial discharge/charge capacity of 1094/801 mAh g⁻¹, relating to an initial Coulombic efficiency (ICE) of 73.2%. Meanwhile, N/P-MoO₂@C0 shows an initial discharge/charge capacity of 890/595 mAh g⁻¹, corresponding to an ICE value of 66.8%. The low ICE may due to the irreversible trapping of Li⁺ in the MoO₂ lattice and the formation of the solid electrolyte interphase (SEI) film.^{12,33} Further works, such as electrolyte optimization, need to be done to improve

the ICE value of N/P-MoO₂@C networks to make it more suitable for practical application. After the first cycle, the capacity of N/P-MoO₂@C4 continues to grow, which is related to a gradual activation process, and a change in the lithiation mechanism from intercalation to conversion dominates the process.^{12,34,35} Fig. S18 confirms the increasing capacity of N/P-MoO₂@C4, which is not obvious in the N/P-MoO₂@C0. After 100 cycles, the N/P-MoO₂@C4 still exhibits a high reversible capacity of 1381 mAh g⁻¹, which is much higher than that of N/P-MoO₂@C0. The rate capabilities of these N/P-MoO₂@C networks are shown in Fig. 2c, where the current density increases step-wisely from 0.05 to 20 A g⁻¹ and then returns to 0.5 A g⁻¹. The specific discharge capacity of N/P-MoO₂@C4 at high current density of 1.0, 3.0, 5.0, 8.0, 10, 15, and 20 A g⁻¹ is 749, 557, 477, 417, 383, 334, and 321 mAh g⁻¹, respectively. Excellent capacity retention of 43.5% is observed in the N/P-MoO₂@C4 on increasing the current density from 1.0 to 20 A g⁻¹. After a deep cycling at 20 A g⁻¹, a very high capacity of 1023 mAh g⁻¹ could be retained after switching the current density back to 0.5 A g⁻¹ at the 50th cycle, indicating the superior structural stability of this novel electrode. The long-life cycling performance of these N/P-MoO₂@C networks was investigated at 20 A g⁻¹ (Fig. 2d). Clearly, both the N/P-MoO₂@C0 and N/P-MoO₂@C4 exhibit good capacity retention over 5000 cycles at a high current density. In particular, the N/P-MoO₂@C4 still delivers capacity of 346 mAh g⁻¹ at the end of the 5000th cycle, corresponding to a near 100% capacity retention. As far as we know, this is the best Li-storage capacity among the reported MoO₂-based^{11,13,14,24,28-32,36} and many other Mo-electrodes shown in Fig. 2e.

The excellent cycle stability and high reversible capacity of the N/P-MoO₂@C4 make it stand out from other competitors as listed in Table S3. Especially, the reversible capacity of N/P-MoO₂@C4 is high than its theoretical value (838 mAh g⁻¹ based on four electron transfer). In order to understand such outstanding Li⁺ storage performance, further studies are carried out. Generally, the total capacity of conversion-type electrode comes from the following three parts: redox reaction, faradaic contribution from the charge transfer with surface atoms, and pseudocapacitance contribution from the double-layer effect.^{37,38} In addition, the existence of pseudocapacitance behavior will also explain the long cycle-life of this N/P-MoO₂@C4 electrode. Therefore, the contribution of pseudocapacitance behavior in the N/P-MoO₂@C networks is investigated, and the power-law relationship is used, as shown in equation (1) and (2).³⁹⁻⁴¹ Herein, i is current (A), v is scan rate (V s⁻¹), a and b are adjustable parameters. The b values can be calculated according to the slope of $\log i$ versus $\log v$ plot. When b approaches to 0.5, the electrode is dominated by a faradic reaction. When b is close to 1, the electrochemical reaction is dominated by a pseudocapacitance behavior. The CV curves that tested at various

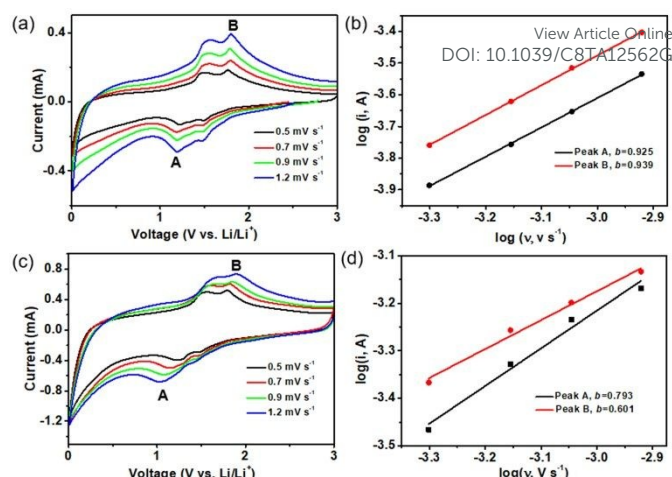


Fig. 3 CV curves at various scan rates and the corresponding $\log i$ versus $\log v$ plot of (a, b) N/P-MoO₂@C4, and (c, d) N/P-MoO₂@C0, respectively.

scan rates and the corresponding $\log i$ versus $\log v$ plot plots are given in Fig. 3. Typical peak A and peak B are selected to investigate the b values during the cathodic and anodic process. As shown in Fig. 3b, the b -values are calculated to be 0.925 and 0.939 for the cathodic and anodic process of N/P-MoO₂@C4, reflecting its remarkable pseudocapacitive effect in enhancing electrochemical performance. For comparison, the b -values are calculated to be 0.793 and 0.601 for N/P-MoO₂@C0, which are also larger than 0.5, but are much lower than those of N/P-MoO₂@C4, indicating a moderate pseudocapacitance behavior of N/P-MoO₂@C0. The high b -values associated with superior pseudocapacitance contribution for the N/P-MoO₂@C4 can be attributed to its more tightly cross-linked nanostructure, higher surface area with abundant smaller mesopores and some micropores,^{14,40-43} and a bit more N and P codoped carbon coating,^{38,41,42} with respect to the N/P-MoO₂@C0. As a result, the enhanced pseudocapacitance behavior for N/P-MoO₂@C4 plays a vital role in contributing to the superior performance in the total electrochemical process.

$$i = av^b \quad (1)$$

$$\log i = b \times \log v + \log a \quad (2)$$

To further confirm the structural advantages of the N/P-MoO₂@C4 for electrochemical energy storage, the sodium storage performance was also explored (Fig. 4). The discharge/charge plots of N/P-MoO₂@C4 at 0.1 A g⁻¹ (Fig. 4a) demonstrate a high initial discharge capacity of 910 mAh g⁻¹, with 300 mAh g⁻¹ retained during the charge process. At the 5th cycle, the discharge and charge capacities are stabilized at high values of 312 and 299 mAh g⁻¹, corresponding to coulombic efficiency (CE) of 95.8%. As expected, the N/P-MoO₂@C4 also exhibits excellent rate performance in SIBs (Fig. 4b), with high capacities ranging from 312 to 175 mAh g⁻¹ at current densities between 0.1 and 0.8 A g⁻¹. Even at 1.0 A g⁻¹, a capacity of 151 mAh g⁻¹ can still be retained, indicating good electrochemical kinetics. Generally, the cycling performance of MoO₂-based electrodes is not satisfactory for SIBs, due to severe volume expansion. Surprisingly, the N/P-MoO₂@C4 electrode can maintain 111 mAh g⁻¹ after 1100 cycles at 1.0 A g⁻¹ (Fig. 4c), indicating good capacity retention of 73.5% and a CE of ~100%.

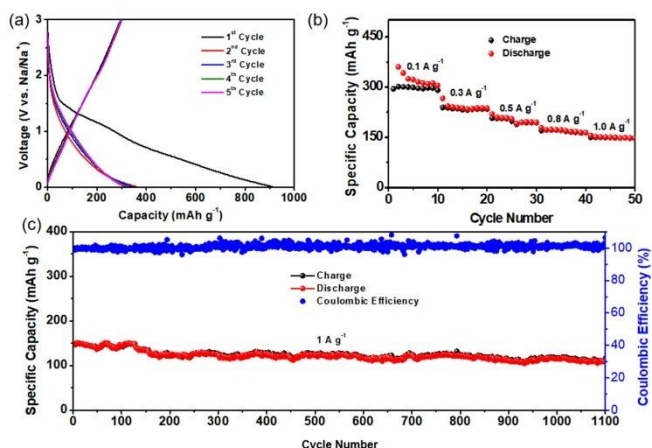


Fig. 4 Sodium storage performance of the N/P-MoO₂@C4 electrode. (a) Galvanostatic charge/discharge profiles at 100 mA h g⁻¹, (b) rate performance at different current densities from 0.1 to 1.0 A g⁻¹, and (c) long-life cycling performance and Coulombic efficiency at 1.0 A g⁻¹.

The unprecedented energy storage performance of this novel N/P-MoO₂@C4 electrode can attribute to the following essentials: (a) The tightly cross-linked tunnels in the N/P-MoO₂@C4 constitute abundant smaller mesopores and micropores within the internal structure, which shortens the ion diffusion pathways and allows more ions to pass through in a given time, leading to a much higher efficiency for ion transfer. Meanwhile, these tunnels also offer multiple channels for electron diffusion, which is beneficial for accelerating the electrochemical kinetics of the electrode.^{5,11,13,14,44} (b) The robust cross-linked porous structure of N/P-MoO₂@C4 also can effectively tolerate volume changes of MoO₂ during the charging/discharging processes.^{29,45,46} (c) This N/P codoped MoO₂@C4 network can not only accommodate the volume changes of MoO₂ as none of the doped or single doped MoO₂@C hybrids do, but also facilitates better electrochemical kinetics due to the synergistic effects between C, N and P.¹⁵⁻¹⁸ In a word, these features dramatically enhance the pseudocapacitance behavior and the kinetics of N/P-MoO₂@C4 for Li⁺ storage/release.

Conclusions

In summary, ionic liquid-based polyoxometalates (IL-POMs) are regarded as molecular precursors for precise synthesis of Mo-based electrodes. By simply adjusting the position of cyano groups in the IL-POMs, we obtain a series of N/P-codoped MoO₂@C networks with distinct N, P and C contents and pore geometry. Excellent energy storage performance is achieved in the N/P-MoO₂@C networks, which synergistically combine the advantages of heteroatom doping, carbon coating, cross-linked conductive mesoporous networks and high pseudocapacitance contributions. In particular, the optimized electrode N/P-MoO₂@C4 demonstrates the highest reversible capacity of 1381 mA h g⁻¹ at 0.5 A g⁻¹, and there is almost 100% capacity retention at 20 A g⁻¹ for 5000 cycles in LIBs. Considerable sodium storage performance is also observed in N/P-MoO₂@C4, in terms of high capacity, good rate capability, and exciting cycling performance. These encouraging results confirm the structural superiority of N/P-MoO₂@C networks as electrodes for both Li⁺ and Na⁺ storage. It is reasonable to deduce that by using IL-POMs as precursors, this facile and large-scale method can pave the way to

the synthesis more Mo- or other metal-based materials towards diverse applications.

DOI: 10.1039/C8TA12562G

Experimental

Materials

4,4'-bipyridine, 4-cyanobenzyl bromide, 3-cyanobenzyl bromide, benzyl bromide, H₃PMo₁₂O₄₀ and the required solvents were commercially available and used as received.

Methods

Liquid-state ¹H and ¹³C NMR spectra were measured with a Bruker DPX 500 spectrometer at ambient temperature in the solvent D₂O using TMS as internal reference. Fourier transform infrared (FTIR) spectra were recorded on a Bruker Vertex 80V instrument (KBr disks) in the 4000-500cm⁻¹ region. XRD patterns were collected on the Bruker D8 Advance powder diffractometer using Ni-filtered Cu Kα radiation source at 40 kV and 20 mA, from 5 to 80° with a scan rate of 0.2° s⁻¹. The morphologies of the samples were characterized using Field-emission scanning electron microscopy (FESEM, Hitachi SU8010), transmission electron microscopy (TEM) and high-resolution TEM (HRTEM, JEOL JEM-2010FEF). N₂ adsorption-desorption isotherms were performed on a Quantachrome autosorb iQ2 at 77 K, and the surface area of samples was calculated using the Brunauer-Emmett-Teller (BET) method and the pore size distribution was determined by the Barrett-Joyner-Halenda (BJH) model and the non-local density function theory (NLDFT), while the samples were degassed at 150 °C for 6 h in a high vacuum before analysis. Thermogravimetric analysis (TGA) was carried out with a TA-Q50 instrument in nitrogen or air atmosphere at a heating rate of 10 °C min⁻¹. The CHN elemental analysis was performed on an elemental analyzer Vario EL cube. Raman spectra were recorded on Renishaw inVia with laser excitation at 514.5 nm. X-ray photoelectron spectroscopy (XPS) was recorded on the Thermo ESCALAB 250XI.

Synthesis of cyano-tethered viologen ionic liquid precursors

In a typical synthesis, D[4-CNbzBPy]Br₂, 1,1'-bis(4-cyanobenzyl)-[4,4'-bipyridium] dibromide, was prepared by treating a homogeneous CH₃CN solution (30 mL) of 4,4'-bipyridine (10 mmol, 1.56 g) and 4-cyanobenzyl bromide (20 mmol, 3.92 g) in a 50 mL Teflon-lined autoclave at 100 °C for 48 h. After reaction, the formed solid was dispersed into CH₃CN solution with vigorous stirring for 2 h. The suspension was filtrated, washed with CH₃CN and ethanol several times, and dried at 80 °C for 12 h in vacuum to give a yellow solid with a yield of 85%.

In a similar process, D[3-CNbzBPy]Br₂, 1,1'-bis(3-cyanobenzyl)-[4,4'-bipyridium] dibromide; D[BzBPy]Br₂, 1,1'-bis(benzyl)-[4,4'-bipyridium] dibromide, were obtained as high-yield (ca. 90%) yellow solids by the replacement of 4-bromobenzyl bromide with 3-bromobenzyl bromide or benzyl bromide.

D[4-CNbzBPy]Br₂, ¹H NMR (300 MHz, DMSO-*d*₆, δ) (Fig. S1A): 9.56~9.58 (CH, 4H), 8.79~8.81 (CH, 4H), 7.68~7.70 (CH, 4H), 7.62~7.64 (CH, 4H), 5.98 (CH₂, 4H); ¹³C NMR (75.5 MHz, DMSO-*d*₆, δ) (Fig. S1B): 149.63, 146.16, 133.89, 132.64, 131.81, 127.69, 123.55, 62.87. Anal. calcd for C₂₆H₂₀N₄Br₂ (MW: 548.27): C 56.96, H 3.68, N 10.22; found: C 56.95, H 3.72, N 10.21.

D[3-CNzBPY]Br₂, ¹H NMR (300 MHz, DMSO-*d*₆, δ) (Fig. S2A): 9.54~9.56 (CH, 4H), 8.15 (CH, 2H), 7.94-8.00 (CH, 4H), 7.68~7.72 (CH, 2H), 5.96~6.03 (CH₂, 4H); ¹³C NMR (75.5 MHz, DMSO-*d*₆, δ) (Fig. S2B): 149.72, 146.43, 135.86, 134.45, 133.65, 133.29, 130.92, 127.72, 118.71, 112.54, 62.85. Anal. calcd for C₂₆H₂₀N₄Br₂ (MW: 548.27): C 56.96, H 3.68, N 10.22; found: C 56.52, H 3.86, N 10.29.

D[BzBPY]Br₂, ¹H NMR (300 MHz, DMSO-*d*₆, δ) (Fig. S3A): 9.60~9.61 (CH, 4H), 8.80~8.82 (CH, 4H), 7.66~7.68 (CH, 4H), 7.46~7.48 (CH, 4H), 7.44~7.45 (CH, 2H), 6.01 (CH₂, 4H); ¹³C NMR (75.5 MHz, DMSO-*d*₆, δ) (Fig. S3A): 149.64, 146.12, 134.67, 129.99, 129.73, 129.46, 127.72, 63.69. Anal. calcd for C₂₄H₂₂N₂Br₂ (MW: 498.25): C 57.85, H 4.45, N 5.62; found: C 56.64, H 4.52, N 5.56.

Preparation of ionic liquid-polyoxometalate (IL-POM) nanohybrids

IL-POM nanohybrids were prepared by the ionic self-assembly of water-soluble viologen ionic liquid precursors with POM such as H₃PMo₁₂O₄₀. In a typical synthesis by using D[4-CNzBPY]Br₂ and H₃PMo₁₂O₄₀, D[4-CNzBPY]Br₂ (0.50 g, 0.912 mmol) was dissolved in deionized water (20 mL) and formed a homogeneous solution with a mass concentration of 5 mg mL⁻¹, and then the equivalent H₃PMo₁₂O₄₀ (1.11 g, 0.608 mmol) aqueous solution (10 mg mL⁻¹) was slowly added into the above IL aqueous solution within 15 minutes. The transparent solution gradually become a yellow green liquid-solid suspension with continuously stirred for 24 h at room temperature. Finally, the yellow green product named as D[4-CNzBPY]_{1.5}PMo was obtained with a yield of 88% after the consecutive basic operations including filtration, washing and drying. Anal. calcd for D[4-CNzBPY]_{1.5}PMo: C 19.47, H 1.26, N 3.49; found: C 20.27, H 1.94, N 3.37.

In a similar process, 3-cyano-contained D[3-CNzBPY]_{1.5}PMo and cyano-free IL-POM hybrid D[BzBPY]_{1.5}PMo was prepared by the reaction of D[3-CNzBPY]Br₂ or D[BzBPY]Br₂ with H₃PMo₁₂O₄₀ in aqueous solution. Anal. calcd for D[3-CNzBPY]_{1.5}PMo: C 19.47, H 1.26, N 3.49; found: C 20.80, H 1.67, N 3.61; Anal. calcd for D[BzBPY]_{1.5}PMo: C 18.56; H 1.43; N 1.80; found: C 20.00, H 1.34, N 1.92.

Preparation of N/P-MoO₂@C networks derived from IL-POM s

In a typical synthesis, 0.5 g IL-POM hybrid D[4-CNzBPY]_{1.5}PMo was placed in a quartz boat and pyrolyzed in a tube furnace. The sample was heated at a temperature of 700 °C at a ramp rate of 10 °C min⁻¹ under nitrogen atmosphere (0.1 L min⁻¹) and maintained at the final temperature for 2 h. Afterward, the tube furnace was slowly cooled down to room temperature to directly produce the black sample N/P-MoO₂@C₄. Similarly, the control samples N/P-MoO₂@C₀ and N/P-Mo₂C@C₃ were prepared by the pyrolysis of D[BzBPY]_{1.5}PMo and D[3-CNzBPY]_{1.5}PMo under the same conditions. Elemental analysis for N/P-MoO₂@C₄: C 5.2, N 1.8; N/P-MoO₂@C₀: C 3.9, N 1.1; N/P-Mo₂C@C₃: C 5.5, N, 1.7.

Electrochemical testing

Electrochemical performance of the sample was evaluated by assembling 2032 coin cell batteries. Typically, active materials, conductive carbon black, and polyvinylidene fluoride (PVDF) were mixed in a weight ratio of 8:1:1, dispersed in N-methyl-2-pyrrolidone (NMP), and then milled for 30 min to form a slurry. The slurry was cast onto copper foils using a doctor blade, and vacuum dried at 80 °C

overnight. The loading amount of the active materials N/P-MoO₂@C networks is about 0.55 mg cm⁻². Lithium discs (MTI Corporation) were used as the counter electrode. 1 M LiPF₆ (Sigma Aldrich) in ethylene carbonate (EC, Sigma Aldrich), diethyl carbonate (DEC, Alfa Aesar), and fluorinated ethylene carbonate (FEC, Sigma Aldrich) (volume ratio 6:3:1) was used as the electrolyte. Polypropylene (PP, MTI Cooperation) was used as the separator. The cells were assembled in an argon-filled glove box with the oxygen and water content below 0.1 ppm. Galvanostatic charge-discharge tests were carried out at room temperature on a battery testing system (LAND Wuhan, China) in a potential range of 0.01~3.00 V (vs. Li/Li⁺). Cyclic voltammetry (CV) tests and electrochemical impedance spectroscopy (EIS) measurements were performed on a CHI660E electrochemical work station.

Conflicts of interest

There are no conflicts to declare

Acknowledgements

We are grateful for financial support from the National Natural Science Foundation of China (21603089, 21805117 and 21503098), the Natural Science Foundation of Jiangsu Province for Youths (BK20160209 and BK20181014), the Natural Science Foundation of the Jiangsu Higher Education Institutions of China (16KJB150014 and 18KJB150015), TAPP, and PAPD.

Notes and references

- L. Ji, Z. Lin, M. Alcoutlabi and X. Zhang, *Energy Environ. Sci.*, 2011, **4**, 2682.
- L. Zhou, K. Zhang, Z. Hu, Z. Tao, L. Mai, Y.-M. Kang, S.-L. Chou and J. Chen, *Adv. Energy Mater.*, 2018, **8**, 1701415.
- W. Li, B. Song and A. Manthiram, *Chem. Soc. Rev.*, 2017, **46**, 3006.
- N. Yabuuchi, K. Kubota, M. Dahbi and S. Komaba, *Chem. Rev.*, 2014, **114**, 11636.
- X. Hu, W. Zhang, X. Liu, Y. Mei and Y. Huang, *Chem. Soc. Rev.*, 2015, **44**, 2376.
- J. H. Ku, J. H. Ryu, S. H. Kim, O. H. Han and S. M. Oh, *Adv. Funct. Mater.*, 2012, **22**, 3658.
- J. Ni, Y. Zhao, L. Li and L. Mai, *Nano Energy*, 2015, **11**, 129.
- X. Zhao, H.-E. Wang, J. Cao, W. Cai and J. Sui, *Chem. Commun.*, 2017, **53**, 10723.
- Y. Wang, L. Yu and X. W. Lou, *Angew. Chem. Int. Ed.*, 2016, **55**, 14668.
- C. Wang, L. Sun, F. Zhang, X. Wang, Q. Sun, Y. Cheng and L. Wang, *Small*, 2017, **13**, 1701246.
- G. Xia, D. Liu, F. Zheng, Y. Yang, J. Su and Q. Chen, *J. Mater. Chem. A*, 2016, **4**, 12434.
- Y. Wang, Z. Huang and Y. Wang, *J. Mater. Chem. A*, 2015, **3**, 21314.
- L. Chen, H. Jiang, H. Jiang, H. Zhang, S. Guo, Y. Hu, C. Li, *Adv. Energy Mater.*, 2017, **7**, 1602782.
- C. Zhao, C. Yu, M. Zhang, H. Huang, S. Li, X. Han, Z. Liu, J. Yang, W. Xiao, J. Liang, X. Sun and J. Qiu, *Adv. Energy Mater.*, 2017, **7**, 1602880.
- J. Zhang, Y. Shi, Y. Ding, L. Peng, W. Zhang and G. Yu, *Adv. Energy Mater.*, 2017, **7**, 1602876.

ARTICLE

Journal Name

- 16 F. Niu, J. Yang, N. Wang, D. Zhang, W. Fan, J. Yang and Y. Qian, *Adv. Funct. Mater.*, 2017, **27**, 1700522.
- 17 Y.-Y. Chen, Y. Zhang, W.-J. Jiang, X. Zhang, Z. Dai, L.-J. Wan and J.-S. Hu, *ACS Nano*, 2016, **10**, 8851.
- 18 L. Ji, J. Wang, X. Teng, H. Dong, X. He and Z. Chen, *ACS Appl. Mater. Interfaces*, 2018, **10**, 14632.
- 19 Y. Leng, J. Wang, D. Zhu, X. Ren, H. Ge and L. Shen, *Angew. Chem. Int. Ed.*, 2009, **48**, 168-171.
- 20 G. Chen, Y. Zhou, P. Zhao, Z. Long and J. Wang, *ChemPlusChem*, 2013, **78**, 561.
- 21 G. Chen, Y. Zhou, Z. Long, X. Wang, J. Li and J. Wang, *ACS Appl. Mater. Interfaces*, 2014, **6**, 4438.
- 22 Y. Zhou, G. Chen, Z. Long and J. Wang, *RSC Adv.*, 2014, **4**, 42092.
- 23 Z. Chen, T. Yang, H. Shi, T. Wang, M. Zhang and G. Cao, *Adv. Mater. Interfaces*, 2017, **4**, 1600816.
- 24 W. Tian, H. Hu, Y. Wang, Peng Li, J. Liu, J. Liu, X. Wang, X. Xu, Z. Li, Q. Zhao, H. Ning, W. Wu and M. Wu, *ACS Nano*, 2018, **12**, 1990.
- 25 X. Yang, Q. Li, H. Wang, J. Feng, M. Zhang, R. Yuan and Y. Chai, *Chem. Eng. J.*, 2018, **337**, 74.
- 26 Y. Zhu, G. Chen, X. Xu, G. Yang, M. Liu and Z. Shao, *ACS Catal.*, 2017, **7**, 3540.
- 27 G. Chen, X. Wang, J. Li, W. Hou, Y. Zhou and J. Wang, *ACS Appl. Mater. Interfaces*, 2015, **7**, 18508.
- 28 J. Pei, H. Geng, H. Ang, L. Zhang, H. Wei, X. Gao, J. Zheng and H. Gu, *Nanotechnology*, 2018, **29**, 295404.
- 29 G. Xu, P. Liu, Y. Ren, X. Huang, Z. Peng, Y. Tang and H. Wang, *J. Power Sources*, 2017, **361**, 1.
- 30 X. Tan, C. Cui, S. Wu, B. Qiu, L. Wang and J. Zhang, *Chem. Asian J.*, 2017, **12**, 36.
- 31 Y. Zhou, H. Xie, C. Wang, Q. He, Q. Liu, Z. Muhammad, Y. A. Haleem, Y. Sang, S. Chen and L. Song, *J. Phys. Chem. C*, 2017, **121**, 15589.
- 32 C. Xia, Y. Zhou, D. B. Velusamy, A. A. Farah, P. Li, Q. Jiang, I. N. Odeh, Z. Wang, X. Zhang and H. N. Alshareef, *Nano Lett.*, 2018, **18**, 1506.
- 33 H.-J. Zhang, J. Shu, K.-X. Wang, X.-T. Chen, Y.-M. Jiang, X. Wei and J.-S. Chen, *J. Mater. Chem. A*, 2014, **2**, 80.
- 34 B. Guo, X. Fang, B. Li, Y. Shi, C. Ouyang, Y.-S. Hu, Z. Wang, G. Stucky and L. Chen, *Chem. Mater.*, 2012, **24**, 457.
- 35 L. Yang, Q. Gao, Y. Zhang, Y. Tang and Y. Wu, *Electrochem. Commun.*, 2008, **10**, 118.
- 36 H.-J. Zhang, K.-X. Wang, X.-Y. Wu, Y.-M. Jiang, Y.-B. Zhai, C. Wang, X. Wei and J.-S. Chen, *Adv. Funct. Mater.*, 2014, **24**, 3399.
- 37 Y. Wang, S. Fan, S. Wu, C. Wang, Z. Huang and L. Zhang, *ACS Appl. Mater. Interfaces*, 2018, **10**, 42372.
- 38 L. Yang, X. Li, Y. Ouyang, Q. Gao, L. Ouyang R. Hu, J. Liu and M. Zhu, *ACS Appl. Mater. Interfaces*, 2016, **8**, 19987.
- 39 T. Brezesinski, J. Wang, S. H. Tolbert and B. Dunn, *Nat. Mater.*, 2010, **9**, 146.
- 40 V. Augustyn, P. Simonbc and B. Dunn, *Energy Environ. Sci.*, 2014, **7**, 1597.
- 41 H.-S. Kim, J. B. Cook, S. H. Tolbert and B. Dunn, *J. Electrochem. Soc.*, 2015, **162**, A5083.
- 42 L. Yang, W. Sun, Z. Zhong, J. Liu, Q. Gao, R. Hu and M. Zhu, *J. Power Sources*, 2016, **306**, 78.
- 43 B. K. Lesel, J. B. Cook, Y. Yan, T. C. Lin and S. H. Tolbert, *ACS Energy Lett.*, 2017, **2**, 2293.
- 44 H. Jiang, X.-C. Liu, Y. Wu, Y. Shu, X. Gong, F.-S. Ke and H. Deng, *Angew. Chem. Int. Ed.*, 2018, **57**, 3916.
- 45 H. Wang, J. Wang, D. Cao, H. Gu, B. Li, X. Lu, X. Han, A. L. Rogach and C. Niu, *J. Mater. Chem. A*, 2017, **5**, 6817.
- 46 X. Xia, S. Deng, D. Xie, Y. Wang, S. Feng, J. Wu and J. Tu, *J. Mater. Chem. A*, 2018, **6**, 15546.

View Article Online
DOI: 10.1039/C8TA12562G

The Table of Contents Entry

Targeted synthesis of ionic liquid-based polyoxometalates derived N/P-codoped MoO₂@carbon porous electrodes with superior lithium and sodium storage performance.

